



HAL
open science

Physical interpretation of the microstructure for aged 12 Cr-Mo-V-W steel creep test samples based on simulation of magnetic incremental permeability

Bhaawan Gupta, Benjamin Ducharne, Gael Sebald, Tetsuya Uchimoto, Takamichi Miyazaki, Toshiyuki Takagi

► To cite this version:

Bhaawan Gupta, Benjamin Ducharne, Gael Sebald, Tetsuya Uchimoto, Takamichi Miyazaki, et al.. Physical interpretation of the microstructure for aged 12 Cr-Mo-V-W steel creep test samples based on simulation of magnetic incremental permeability. *Journal of Magnetism and Magnetic Materials*, 2019, 486, pp.165250. 10.1016/j.jmmm.2019.165250 . hal-02166924

HAL Id: hal-02166924

<https://hal.science/hal-02166924>

Submitted on 22 Oct 2021

HAL is a multi-disciplinary open access archive for the deposit and dissemination of scientific research documents, whether they are published or not. The documents may come from teaching and research institutions in France or abroad, or from public or private research centers.

L'archive ouverte pluridisciplinaire **HAL**, est destinée au dépôt et à la diffusion de documents scientifiques de niveau recherche, publiés ou non, émanant des établissements d'enseignement et de recherche français ou étrangers, des laboratoires publics ou privés.



Distributed under a Creative Commons Attribution - NonCommercial 4.0 International License

Physical Interpretation of the Microstructure for aged 12 Cr-Mo-V-W Steel Creep Test Samples based on Simulation of Magnetic Incremental Permeability

Bhaawan Gupta^{1, 2, 3}, Benjamin Ducharne^{2*}, Gael Sebald¹, Tetsuya Uchimoto^{1, 3}, Takamichi Miyazaki⁴, Toshiyuki Takagi^{1,3}

¹ELyTMaX UMI 3757, CNRS – Université de Lyon – Tohoku University, International Joint Unit, Tohoku University, Sendai, Japan

²Univ Lyon, INSA-Lyon, LGEF, EA682, F-69621, Villeurbanne, France

³Institute of Fluid Science, Tohoku University, Sendai, Japan

⁴Instrumental Analysis Group, Graduate School of Engineering, Tohoku University, Sendai, Japan

Abstract: Magnetic Incremental Permeability (MIP) being highly stress dependent proves to be very effective to evaluate materials non-destructively. In this article, modelling technique based on Jiles-Atherton model has been proposed to simulate the signature MIP butterfly loop for the 12 Cr-Mo-V-W creep test samples. Jiles-Atherton parameters imply physical interpretations. From these butterfly loops, a physical relation, based on the values of the J-A's parameters, with the microstructure such as precipitations, dislocations, Kernel Average Misorientation (KAM) has been investigated with experimental as well as simulation validations. It is especially observed that J-A's parameters are well correlated to the precipitation quantity and KAM.

Keywords: Magnetic incremental permeability, Jiles-Atherton model, creep, micro magnetic non-destructive testing.

1. Introduction

Creep damage occurs in metallic parts due to continuous exposure to very high temperatures and stress. It is a time-dependent phenomenon which may lead to a creep failure [1]. Similarly, residual stresses occur in the metallic parts due to industrial machining and the

*Corresponding author.

E-mail address: benjamin.ducharne@insa-lyon.fr (Benjamin Ducharne)

31 prolonged heat treatments. Consequently, these residual stresses also lead to the part failures
32 resulting to the safety issues. Hence, non-destructive testing techniques are required to
33 monitor the continuous degradation of the materials. Magnetic inspection methods being easy
34 to implement have found a major application and interest in the NDT [1][2]. Magnetic
35 incremental permeability (MIP) being very highly stress and microstructure dependent is a
36 very interesting method to monitor such phenomenon. Experimental methods to address these
37 issues have been proposed [2], and require further investigations to propose relevant standards
38 due to the diversity of experimental setups (such standards are missing). Alternatively, an
39 attractive solution would be to propose simulation techniques to model MIP signature curves
40 (becoming independent from experimental setup) and to derive from it the physical
41 interpretations about the microstructure properties such as the carbide precipitations,
42 dislocations etc.

43 Many investigations around 3D ferromagnetic models and their incremental permeability
44 simulation mainly focus on coupling Space Discretization Techniques (SDT), Finite Elements
45 Method (FEM) or Finite Differences Method (FDM) extended with accurate scalar or vector,
46 dynamic or static hysteresis material law [3][4]. For this magnetic material law, it seems that
47 the best results come from the extension of the quasi-static hysteresis model (Preisach model
48 [5], Jiles-Atherton model [6]) to dynamic behaviour as a result of the separation losses
49 techniques as proposed by Bertotti [7]. In this article, a simulation method based on Jiles-
50 Atherton (J-A) model is proposed. J-A model focuses on its 5 parameters which are related to
51 the physical behaviour of the materials [6]. In this study, simulations are based on the material
52 investigated which is high chromium creep test samples in this study (12 Cr-Mo-W-V) with
53 different temperature, stress levels and rupture times. High chromium steel is chosen for this
54 study as a result of industrial requirement by thermal power plants and requiring more

*Corresponding author.

E-mail address: benjamin.ducharne@insa-lyon.fr (Benjamin Ducharne)

55 investigations compared to low alloy steels [1]. Additionally, creep is a very complex
56 phenomenon to understand, and hence this work is an attempt to understand the creep
57 phenomenon through its effect on magnetic properties.

58 When a ferromagnetic material is exposed to a **quasi-static magnetic field, for a fixed**
59 **operating point in the hysteresis curve**, the reversible permeability measured **when**
60 **superimposing** a small alternative magnetic field is defined as the magnetic incremental
61 permeability [8],

62 Mathematically, magnetic incremental permeability, μ_{Δ} can be defined as [9]

$$63 \quad \mu_{\Delta} = \frac{1}{\mu_0} \frac{\Delta B}{\Delta H} \quad (1)$$

64 where μ_0 is the permeability of vacuum, ΔB is the **resulting** magnetic flux density **when** ΔH is
65 the incremental **driving small** magnetic field.

66 By measuring the minor loop magnetic flux density during the process of magnetization, **MIP**
67 **is calculated as inclination of the minor loop**. As the microstructure of a ferromagnetic
68 material, **directly influencing the magnetic domain structure**, is easily affected by mechanical
69 damage such as plastic deformation and fatigue damage, MIP method is considered as a
70 potential NDT technique to evaluate **the microstructure changing phenomena as well as the**
71 **induced residual stress** [8]. Hence, modelling becomes even more important to understand the
72 behaviour of the material at a deeper level, thereby reducing the experimental efforts and the
73 complicated experimental set-ups.

74 In the second section, the basics of MIP are defined followed by the experimental conditions
75 and procedure. In section 3, the theory of the model is defined in details and how this model is
76 adapted to our samples is demonstrated. Finally, in the section 4, results are discussed in
77 correlation to the microstructure.

*Corresponding author.

E-mail address: benjamin.ducharne@insa-lyon.fr (Benjamin Ducharne)

78

79

80 2. Experimental procedure

81 2.1. Experimental set-up

82 In order to model the MIP curve, there are certain experimental conditions which are
83 considered. MIP is a phenomenon that exists when a high frequency alternating magnetic
84 field is superimposed on to a **quasi-static** magnetic field. In the experimental set-up, a
85 sinusoidal alternating magnetic field (**0.1 Hz**) is applied using a U-shaped electromagnet to
86 the test specimen with an amplitude of 10^4 A/m. A transmitter-receiver (T-R) type coil is used
87 to supply a high frequency magnetic field (**50 KHz**) to superimpose on the **quasi-static**
88 magnetic field. The pick-up coil (receiver, lower coil in Fig. 1) is fed to a digital lock –in
89 amplifier (NF LI 5496) whose output **provides the complex values (real/imaginary part or**
90 **amplitude/phase) of the induced voltage**. For the data acquisition LabVIEW™ is used. The
91 absolute value of the voltage is proportional to the magnetic incremental permeability in the
92 material. When this output voltage is plotted against the applied **quasi-static** magnetic field H
93 **(the output of the Hall sensor is amplified and filtered with a 30 Hz cut off frequency low pass**
94 **filter in order to reduce the surrounding noise)**, it results in the typical butterfly loops as
95 shown in Fig.1 below. The schematic of the experimental set-up is illustrated in Fig.1. It has
96 to be noted that experimentally, the output voltage of the lock-in amplifier is used for MIP
97 curves but from the modelling point of view, we calculate incremental permeability from
98 experimental **time dependent voltage** of the measurement coil. **Since we measure electrical**
99 **signals but simulate magnetic properties hence a link must be established between these**
100 **physical quantities (section 4.3).**

101

*Corresponding author.

E-mail address: benjamin.ducharne@insa-lyon.fr (Benjamin Ducharne)

102

103

104

105

106

107

108

109

110

111

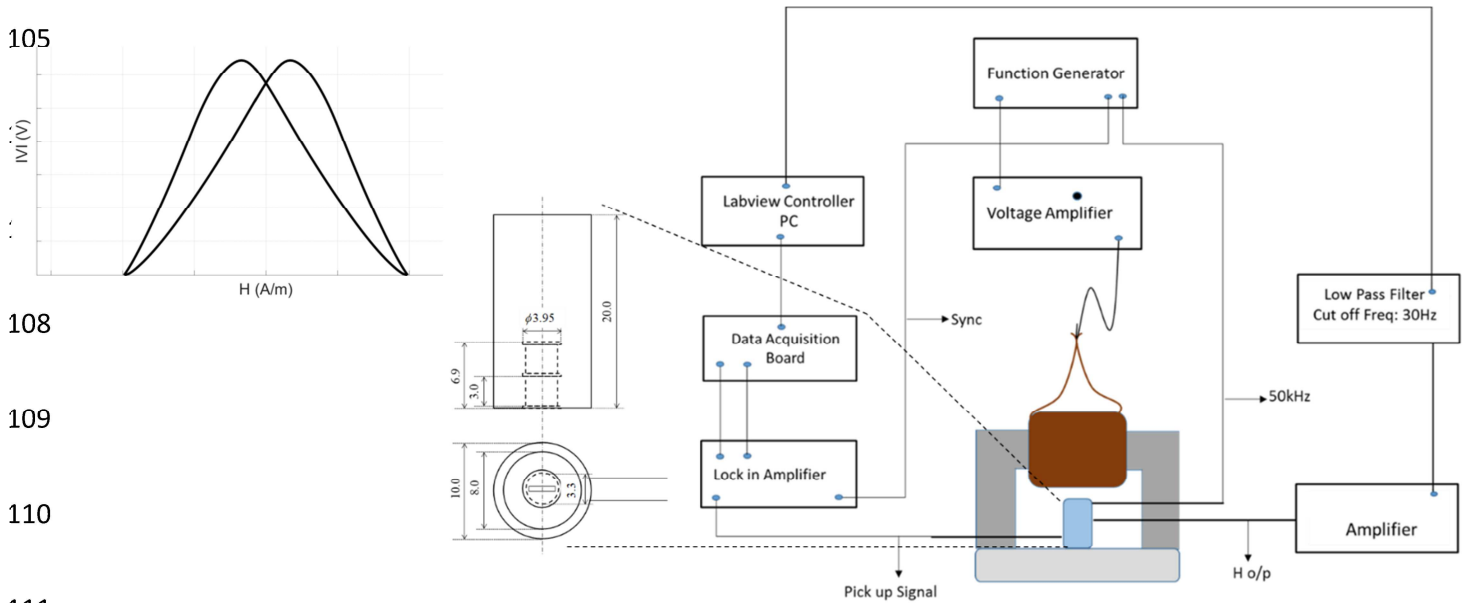


Figure 1: Experimental set-up

112

2.2. Sample description

113

12 Cr-Mo-W-V high chromium steel in this study is used in thermal power plants (Fig. 2).

114

The schematic of the raw sample is shown on the right side of Fig. 2. It is a rod like specimen

115

from which the grip part at the edges is cut after the creep test. Finally, the surface is

116

machined as shown in the left part of the Fig. 2. The samples were cut in this shape so as to

117

make the measurements convenient according to the set up. The magnetic incremental

118

permeability measurement method is applied to creep damage evaluation of high chromium

119

steel (12Cr-Mo-W-V steel) and the possibility of evaluation is investigated in this study. 12%

120

Cr-Mo- W-V Steel is one of the representative martensitic stainless steels, that is majorly used

121

for high temperature materials application in steam and gas turbines, and boilers. The general

*Corresponding author.

E-mail address: benjamin.ducharne@insa-lyon.fr (Benjamin Ducharne)

122 composition of this alloy can be referred in [10]. However, in this case, the percentage of each
123 composition may vary a little bit but the magnetic behaviour will not change significantly.

124

125

126

127

128

129

130

131

132

133

134

135

136

137

138

139

140

141

142

143

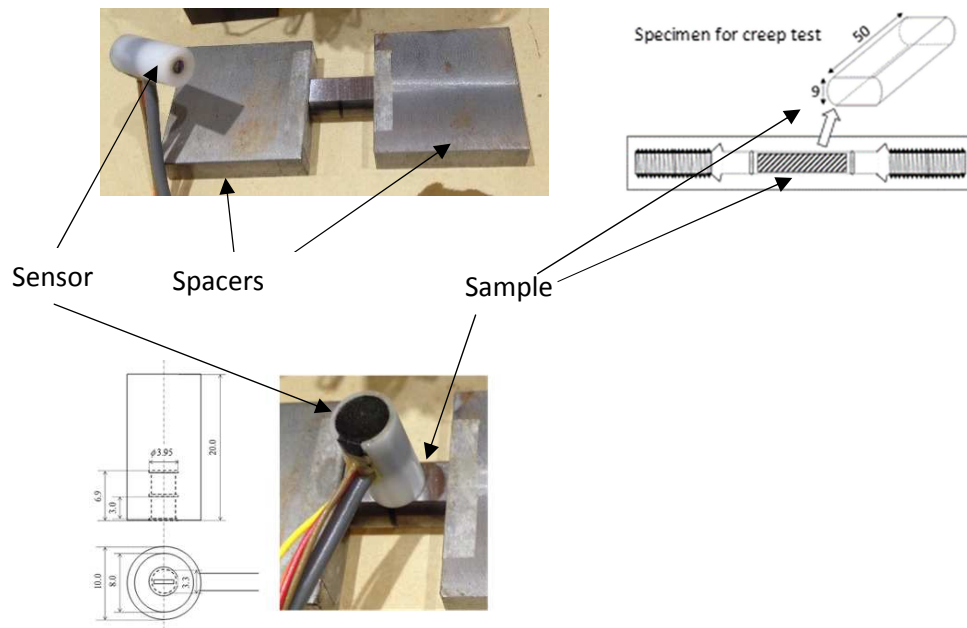


Figure 2: Samples with the sensor probe used

144 Table 1 shows the different samples which are studied in this article with three major
145 categories. Sample 0 is a virgin sample with no damage or treatment. Sample 1, 2 and 3 fall
146 under the category of same temperature treatment of 550 °C and same mechanical treatment
147 of stress level of 343 MPa. These are further sub-categorized on the basis of their times when
148 they were under test. Sample 3 which has a rupture time of 2205.7 hours implying that after
149 2205.7 hours under test, this sample got ruptured. The second category of samples is with a
150 mechanical stress level of 201 MPa and temperature treatment of 600°C. The third category is
151 with the mechanical stress level of 98 MPa and a temperature treatment of 650°. In Table 1,
152 the last column is Larson Miller Parameter (LMP), which is derived from a formula for
153 evaluation of creep [11].

*Corresponding author.

E-mail address: benjamin.ducharne@insa-lyon.fr (Benjamin Ducharne)

154
$$LMP = T(C + \log t), \tag{2}$$

155 Where, C is a material specific constant, often approximated as 20, t is the time in hours and
156 T is the temperature in Kelvins.

157

158

159

Table 1: High chromium steel samples with varied treatments

160

Sample number	Stress [MPa]	Temp [°C]	Test time [h]	LMP*
0	0	0	0.0	0.0
1	343	550	281.8	18479
2	343	550	785.6	18846
3	343	550	2205.7	19215
4	201	600	255.6	19565
5	201	600	763.9	19980
6	201	600	1725.9	20289
7	98	650	256.3	20686
8	98	650	789.6	21137
9	98	650	1736.8	21453

161

162

163

164

165

166

167

**Larson Miller Parameter*

168 As we know that after rupture, high plastic deformation, necking of geometry and even micro
169 porosity can be observed close to the ruptured area, hence to make sure that all our samples
170 are investigated in the same conditions, all the tests have been performed far from the
171 ruptured area.

172 **2.3. Electron Backscatter diffraction and Scanning Electron Microscopy Analysis**

173

174 In this section, the microstructural analysis has been illustrated with Scanning Electron
175 Microscopy (SEM) imaging technique followed by the Electron backscatter diffraction
176 (EBSD) observation. EBSD data was analysed using OIM software. Using EBSD, Kernel
177 Average Misorientation (KAM) data are obtained. The KAM is the average misorientation
178 angle of a given point with all its neighbours [12]. When a crystalline material undergoes
179 plastic deformation, the crystalline lattice becomes rearranged to compensate for the

*Corresponding author.

E-mail address: benjamin.ducharne@insa-lyon.fr (Benjamin Ducharne)

180 geometric changes in the material. The samples are prepared by the combination of sawing
 181 and cutting to prepare small specimens which are then mechanically polished to ensure
 182 smooth-flat surfaces, while reducing mechanical damage. The ultimate polishing powder is
 183 used at #8,000. Ar-ion milling method is used to remove any strain hardening at a preliminary
 184 mechanical preparation. The Ar-ion beams are directed towards the sample surface at lower
 185 angle (3-4 degree). This procedure is explained well in the previous version of this article [13]
 186 along with the interpretations of the SEM as well as EBSD images. Standard procedures could
 187 also be referred in [14] [15]. The statistical analysis of the microstructure (Precipitation
 188 Number & Average of Kernel Average Misorientation) vs. the magnetic parameters is
 189 demonstrated in Fig.3-4. Fig. 5 shows a typical MIP curve and some of the parameters
 190 highlighted that can be derived from the magnetic curve.

191

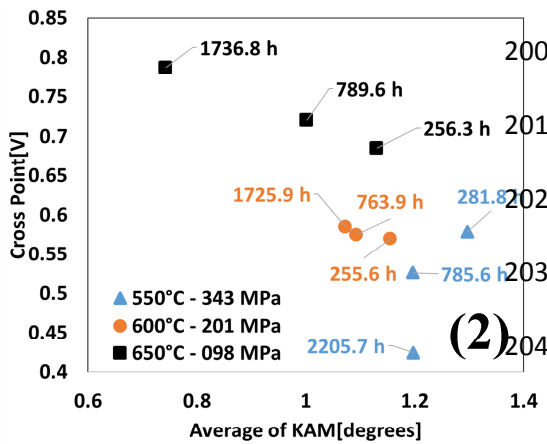
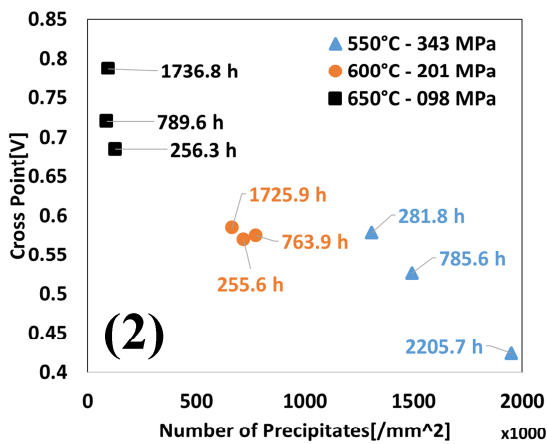
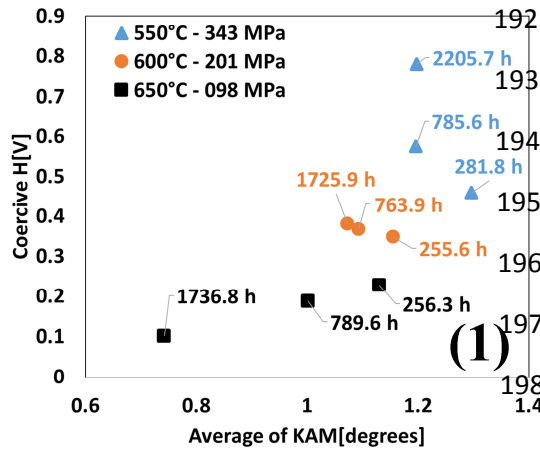
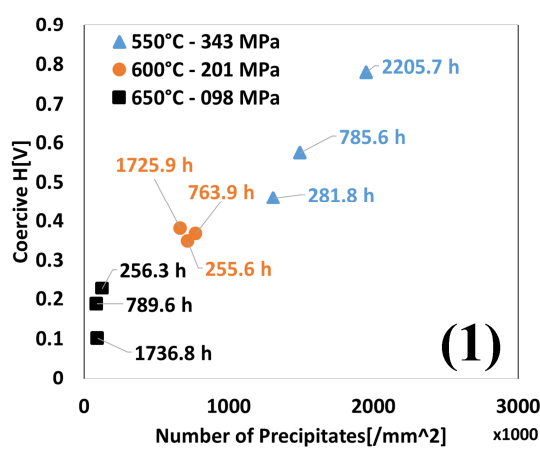
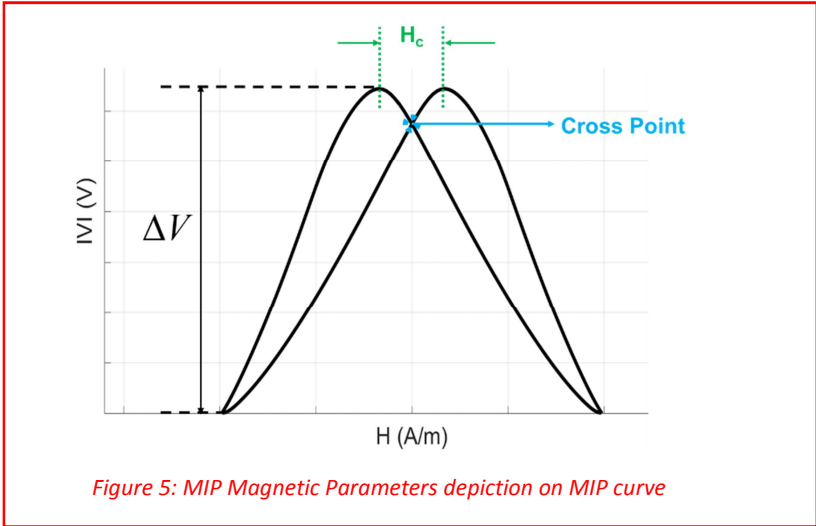


Figure 3: Data evaluation of different magnetic parameters against number of precipitates

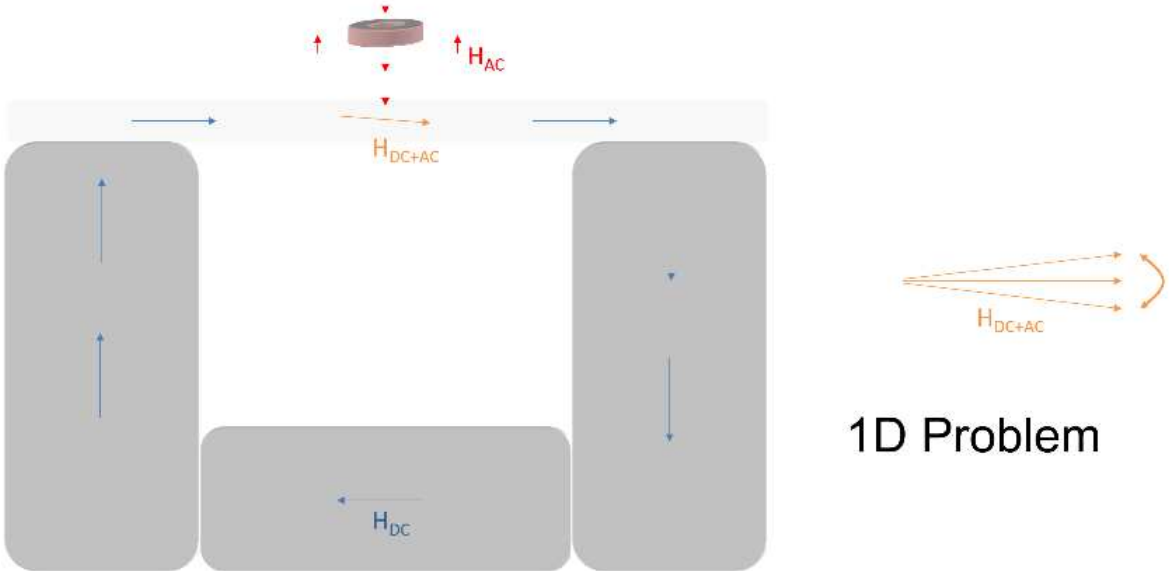
Figure 4: Data evaluation of different magnetic parameters against Average of KAM

205
206
207
208
209
210
211
212
213
214
215
216
217
218
219
220
221
222
223
224
225
226



3. Theory and Modeling
3.1. Lump model

In this part of the article, a mathematical model based on physical properties is proposed to simulate the material behavior under magnetic incremental permeability (MIP) situation. In a comprehensive approach, a full 3D magnetic model is required to take into account the different axial components of the magnetic field as well as being able to simulation inhomogeneous field distribution. Alternatively, a simplifying assumption can be used to focus on a scalar analytical model, assuming B and H collinear.



*Corresponding E-mail address

227

Figure 5 – Illustration of the vector magnetic field distribution.

228 In the classic MIP set-up, both excitation contributions are **perpendicular** vector quantities but
229 the quasi-static excitation field **maximum** amplitude is typically 1000 times higher than the
230 AC one. Consequently in the scanned area the direction of the vector cumulative excitation
231 field \vec{H} ($\vec{H}_{DC} + \vec{H}_{AC}$ contribution) remains **almost** constant **during a large proportion of the**
232 **quasi-static magnetization process. According to this observation and to simplify the**
233 **simulation scheme**, the \vec{H} vector is then assumed collinear to the induction \vec{B} one. Based on
234 this assumption, a scalar **approach** with accurate scalar hysteretic material law **is considered**
235 **for the simulation of the material magnetic behavior**. In addition, working with a low enough
236 H_{DC} frequency, **the induced magnetization behavior is homogeneous in the material under test**.
237 The dynamic excitation H_{AC} is concentrated on the vicinity of the measurement coils and in
238 the surface of the sample. As it is of very small amplitude, it is assumed the permeability is
239 constant, so that the measured voltage amplitude remains proportional to the permeability.
240 The AC magnetic field amplitude is extremely weak and even at 50 kHz, the local excitation
241 slope dH/dt due to the AC field is assumed to be lower than the maximum of dH/dt observed
242 below the quasi static threshold. **Consequently, no dynamic contribution will be taken into**
243 **account in our simulation. This assumption is validated by experimentally by increasing the**
244 **AC frequency and observing no significant variations on the resulting MIP curve**.
245 In this study, we focus on simulating the variations of the permeability modulus versus the
246 magnetic excitation field (MIP signature curve). A dynamic contribution during the minor
247 loop situations would affect the phase shift between B and H as it is explained in [16]- [18]
248 but would have very less influence on the permeability modulus (**MIP signal**).
249 Consequently, no dynamic contributions are considered in the simulations. If the objective is
250 to simulate the butterfly loop $|\mu|(H)$, then a quasi-static contribution is enough to achieve

*Corresponding author.

E-mail address: benjamin.ducharne@insa-lyon.fr (Benjamin Ducharne)

251 good simulation result. For this quasi-static contribution, there are two options: Firstly, a
252 modified Jiles-Atherton model [6][19]-[21], where the accommodation issue (i.e. it takes
253 many cycles for a minor hysteresis loop to stabilize) is solved by considering the AC field
254 amplitude sufficiently weak to ignore hysteresis during the minor loop situation. Secondly, a
255 modified “applied H dependent” type model, such as the Preisach model [5] or the dry friction
256 model [22] can be considered. Such models are congruent, which means that when a
257 ferromagnetic sample is cycled between two magnetic excitation levels, the size and shape of
258 the resulting minor remanence loop predicted does not depend upon the magnetic state of the
259 system. This phenomenon leading to a butterfly loop limited to a single anhysteretic curve is
260 solved by considering $H_{eff} = H(t) + \alpha \cdot B(t)$ instead of H as input of the model. H_{eff} is the
261 effective field whereas α is a proportionality constant between the average field and the
262 magnetization. These two approaches are both relevant. In our work, the modified Jiles-
263 Atherton model was chosen for its limited number of parameters and their physical
264 interpretation.

265

266

267

268

269 **3.2. The Jiles-Atherton model**

270 **3.2.1. Introduction and classic use of the Jiles-Atherton model**

271 Below a threshold frequency, the cumulative periodic value of the ferromagnetic losses
272 becomes frequency-independent. This particular behavior is called the quasi-static state.

*Corresponding author.

E-mail address: benjamin.ducharne@insa-lyon.fr (Benjamin Ducharne)

273 The J-A model is based on the consideration of two contributions – the domain walls bending
274 and the domain wall translations. It should be noted that the J-A model exhibits some
275 particularly interesting features as follows.

- 276 • The required memory allocation is less.
- 277 • Its status can be completely described by only five parameters.
- 278 • The five parameters are related to the microstructural property, which allows a
279 physical interpretation of the J-A model.
- 280 • The J-A model is easily reversible and relatively easy to switch from H to B as the
281 input for the quasi-static hysteresis model.

282 In the first version of the scalar J-A model for ferromagnetic materials, the total magnetization
283 M is decomposed into its reversible (M_{rev}) and irreversible (M_{irr}) contribution. From a physical
284 point of view M_{rev} is associated to the magnetic domains rotation and M_{irr} to the wall
285 displacements.

$$286 \quad M = M_{rev} + M_{irr} \quad (3)$$

287 The anhysteretic magnetization M_{anh} can be described by the Langevin equation [23]:

$$288 \quad M_{anh} = M_s \left[\coth \left(\frac{H_e}{a} \right) - \frac{a}{H_e} \right] \quad (4)$$

289 or using a hyperbolic function:

$$290 \quad M_{anh} = M_s \tanh \left(\frac{H_e}{a} \right) \quad (5)$$

291 In both equations (4) and (5), M_{anh} is the anhysteretic magnetization, H_e is the effective field,
292 M_s is the saturation magnetization and a is the **anhysteretic magnetization shape parameter**.
293 According to J-A theory $a = k_B \cdot T / \mu_0 \cdot m$ in which k_B is Boltzmann's constant, T is the
294 temperature, and m is the magnetic moment of a typical domain.

*Corresponding author.

E-mail address: benjamin.ducharne@insa-lyon.fr (Benjamin Ducharne)

295
$$H_e = H + \alpha.M \quad (6)$$

296

297 Here, H is the applied excitation field (tangent to sample's surface), M the average sample
 298 magnetization and α , a mean field parameter related to the inter domain coupling (see J-A
 299 theory [6][19]-[21]). The anhysteretic, the irreversible and reversible magnetization are linked
 300 in equation (7):

301
$$M_{rev} = c(M_{an} - M_{irr}) \quad (7)$$

302 c is a proportionality coefficient. It can be determined using the experimental results by
 303 calculating the ratio of the initial differential susceptibilities of the first and anhysteretic
 304 magnetization curves [6][19]-[21].

305 The derivative of irreversible magnetization with effective field is given by

306
$$\frac{dM_{irr}}{dH_e} = \frac{M_{anh} - M_{irr}}{k\delta} \quad (8)$$

307 The coefficient k is the pinning parameter, according to the J-A's theory it quantifies the
 308 average energy required to break pinning site in the magnetic material, and δ is a directional
 309 parameter which ensures that energy is always lost through dissipation [6][19]-[21].

310
$$\begin{cases} \delta = +1 & \text{if } dH / dt \geq 0 \\ \delta = -1 & \text{if } dH / dt < 0 \end{cases} \quad (9)$$

311 Combining the equations above, the main equation of the J-A model can be written as:

312
$$\frac{dM}{dH} = \frac{(1-c) \frac{dM_{irr}}{dH_e} + c \frac{dM_{anh}}{dH_e}}{1 - \alpha(1-c) \frac{dM_{irr}}{dH_e} - \alpha c \frac{dM_{anh}}{dH_e}} \quad (10)$$

313 The differential equation (10) allows to calculate the variations of the magnetization M with
 314 respect to H variations. However, for some applications B imposed quasi-static model are
 315 required. Ref. [24][25] details the inverse version of the J-A model for the ferromagnetic

*Corresponding author.

E-mail address: benjamin.ducharne@insa-lyon.fr (Benjamin Ducharne)

316 materials, i.e. where the model input is the magnetization B . The physical principles of the
 317 model are very similar and the main equation of this inverse model for ferromagnetic
 318 materials becomes:

319

$$320 \quad \frac{dM}{dB} = \frac{(1-c) \frac{dM_{irr}}{dB_e} + \frac{c}{\mu_0} \frac{dM_{anh}}{dH_e}}{1 + \mu_0(1-\alpha)(1-c) \frac{dM_{irr}}{dB_e} - c(1-\alpha) \frac{dM_{anh}}{dH_e}} \quad (11)$$

321 With

$$322 \quad \frac{dM_{irr}}{dB_e} = \frac{M_{anh} - M_{irr}}{\mu_0 k \delta} \quad (12)$$

323 And

$$324 \quad B_e = \mu_0 \cdot H_e \quad (13)$$

325

326 B_e is the effective magnetic flux density.

327

328

329

330

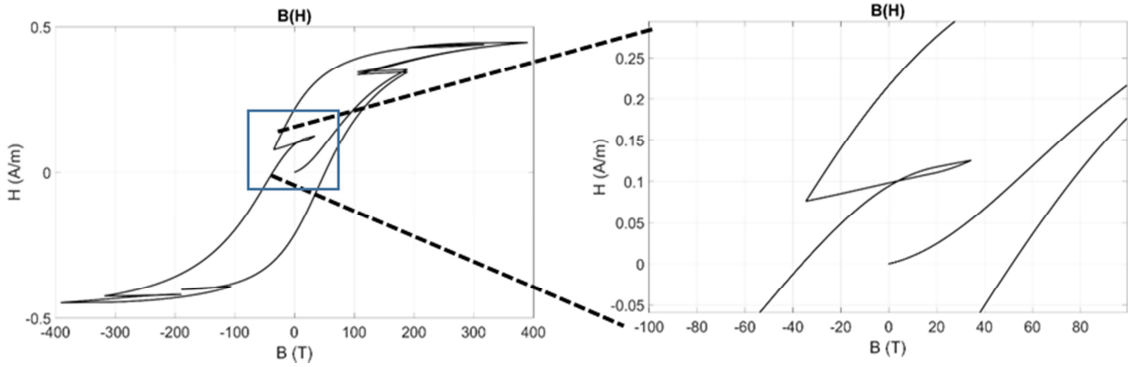
331

332 **3.2.2. The modified Jiles-Atherton model for the simulation of MIP**

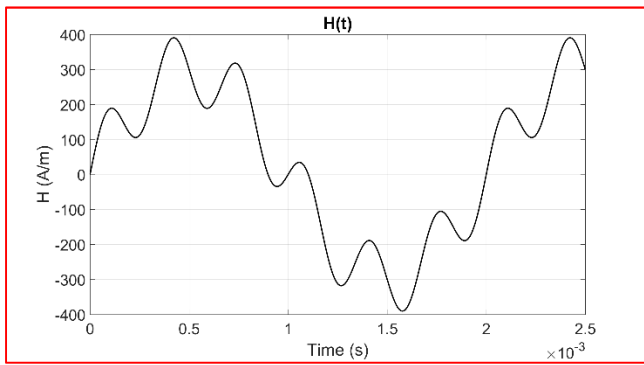
*Corresponding author.

E-mail address: benjamin.ducharne@insa-lyon.fr (Benjamin Ducharne)

333 Under minor loops situation, the classic J-A model presents a slow accommodation time, i.e.
 334 the magnetization trajectory between the turning points of a minor loop will not be closed at
 335 the end of its excursion (Fig. 6).



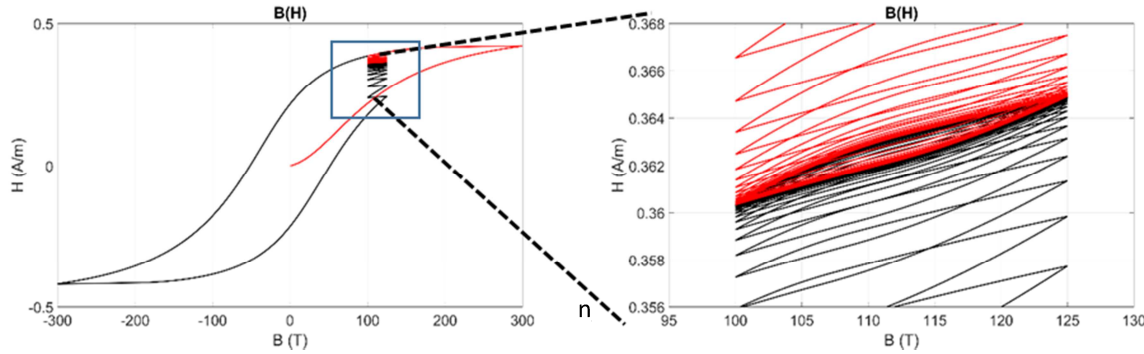
336



337

338 *Figure 6 – Illustration of the accommodation issue with the J-A model under unsymmetrical excitation H .*

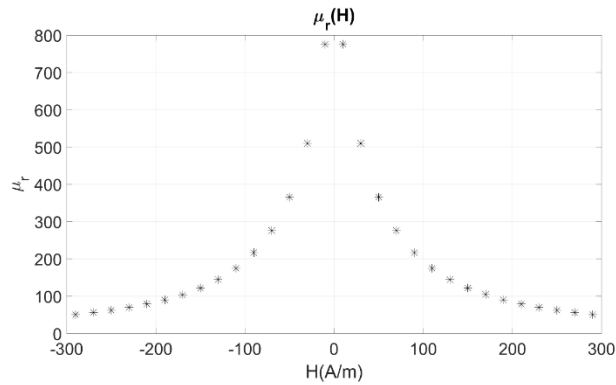
339 It might be assumed that this is just a transient phase and by exciting the ferromagnetic
 340 material with a large number of periods, a steady state will be reached (Fig. 7). This is the
 341 case but the steady state reached is only H dependent and not on the magnetization state.
 342 Consequently, the butterfly loop, evolution of the permeability modulus $|\mu|$ versus H
 343 (signature of the MIP characterization) is just an anhysteretic curve (Fig. 8), far from the
 344 experimental observation.



345

Figure 7 – Illustration for the transient phase under minor loop situation with the J-A model.

346



347

348

349

350

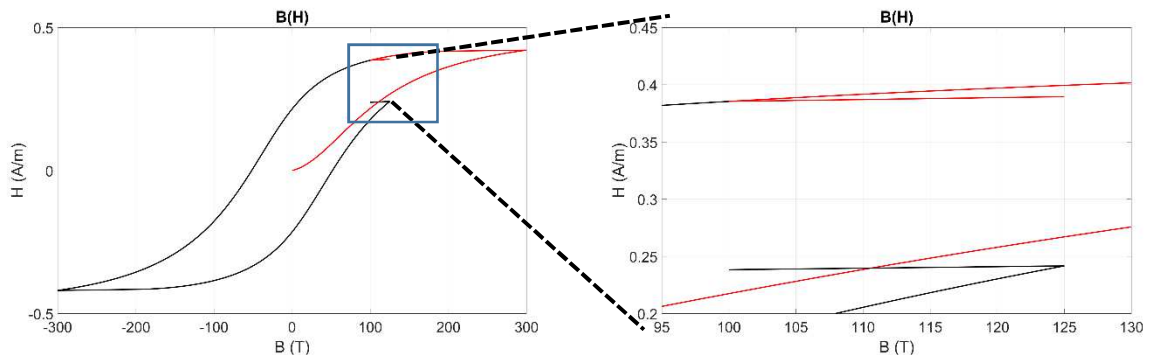
351

Figure 8 – Illustration for the transient phase under minor loop situation with the J-A model.

352 To solve this accommodation issue, $|\overline{H_{AC}}|$ is assumed to be sufficiently weak and by ignoring
 353 the hysteretic behavior during the minor loop situation. Minor cycles are then treated as a
 354 single slope [26][27] (Fig. 9).

355

356



357

358

359

Figure 9 – Illustration for the single slope consideration under minor loops situation.

360 The $|\mu|$ versus H butterfly loop obtained is then very similar to the experimental one and the 5
 361 J-A parameters can be used as degree of freedom in the simulation process.

362

363

364 3.3. Magnetic and electric quantities interdependence

*Corresponding author.

E-mail address: benjamin.ducharne@insa-lyon.fr (Benjamin Ducharne)

365 The experimental setup provides time variations of both the excitation field $H(t)$ and the
366 sensor secondary coil voltage $V(t)$. The numerical simulation as described previously can only
367 provide the times variations of magnetic quantities like the excitation field $H(t)$, the magnetic
368 field $B(t)$ and the permeability $\mu(t)$. To validate the model by comparing it to the experimental
369 results, a link between the electrical and the magnetic quantities must be assigned.

370 A reluctance/impedance lump-type model typography has been used to link both the electrical
371 and magnetic quantities. Both magnetic and air type reluctances are necessary for the
372 simulation of the inductance. Assuming the air reluctance as highly superior to the magnetic
373 one and reducing the equations according to this, a relation can be established between the
374 time variations of both the real and imaginary part of the complex permeability and the sensor
375 voltage as:

$$376 \quad V^* = j\lambda_1 + \lambda_2(-\mu'' + j\mu') \quad (14)$$

377 Here λ_1 , λ_2 , are constants depending on the geometry and on the nature of the material. It is
378 worth noticing that the real part of the voltage is linked to imaginary part of the permeability
379 and reciprocally the imaginary part to the voltage real part. These constants are obtained by
380 comparisons simulations/measures using experimental results performed on a virgin sample
381 **as it is considered our reference sample**. Once set, they are conserved for all others
382 simulations results

383 **3.4. Optimization of the model parameters**

384 To converge with our simulation, a total of 7 parameters must be determined. M_s , a , α , k , c ,
385 and the magnetic/electric parameters λ_1 , λ_2 are obtained by comparing simulations with virgin
386 sample experimental results. Once these parameters are set, they will be conserved for all the
387 samples tested. For the J-A model parameters, the first step consists of calculating the average

*Corresponding author.

E-mail address: benjamin.ducharne@insa-lyon.fr (Benjamin Ducharne)

388 value H_i^{ave} of H_i^{inc} and H_i^{dec} for every given B_i of every sample's major hysteresis cycle
 389 $B(H)$:

$$390 \quad H_i^{ave}(B_i) = \frac{H_i^{inc}(B_i) + H_i^{dec}(B_i)}{2} \quad (15)$$

391 Where H_i^{inc}/H_i^{dec} stands for the H value read on the increasing/decreasing part of the major
 392 hysteresis cycle. The $H_i^{ave}(B_i)$ curve obtained can be considered as relatively close to the real
 393 anhysteretic curve. M_s and a , the J-A anhysteretic parameters are calculated by fitting this
 394 curve to the simulated one using Matlab™ curve fitting toolbox. It is worth noticing that first
 395 optimized relatively correct simulation results have been obtained with extremely weak
 396 variations of both M_s and a , the anhysteretic parameters. In the final approach both these
 397 coefficients are set and the optimization process just focuses on the remaining 3 parameters.
 398 All the constant parameters used for the simulation are displayed Table 2.

399

Table 2: Simulation constant parameter values

$a(\text{A/m})$	$M_s(\text{A/m})$	λ_1	λ_2
10020	2.00E+06	12.9	0.0453

400

401 Finally, comparisons simulation / experimental MIP butterfly loops are used for the calculus
 402 of the 3 remaining coefficients. A dedicated error function is proposed for the calculus of
 403 these coefficients. The 3 parameters α , k and c are set when their combination minimizes this
 404 error function:

$$405 \quad \begin{aligned} & dH / dt > 0, \quad H \in [H_{\min}, H_{\max}] \\ & Error = \sum_{i=1}^n abs(|\mu|_i^{\text{exp}}(H_i) - |\mu|_i^{\text{sim}}(H_i)) \end{aligned} \quad (16)$$

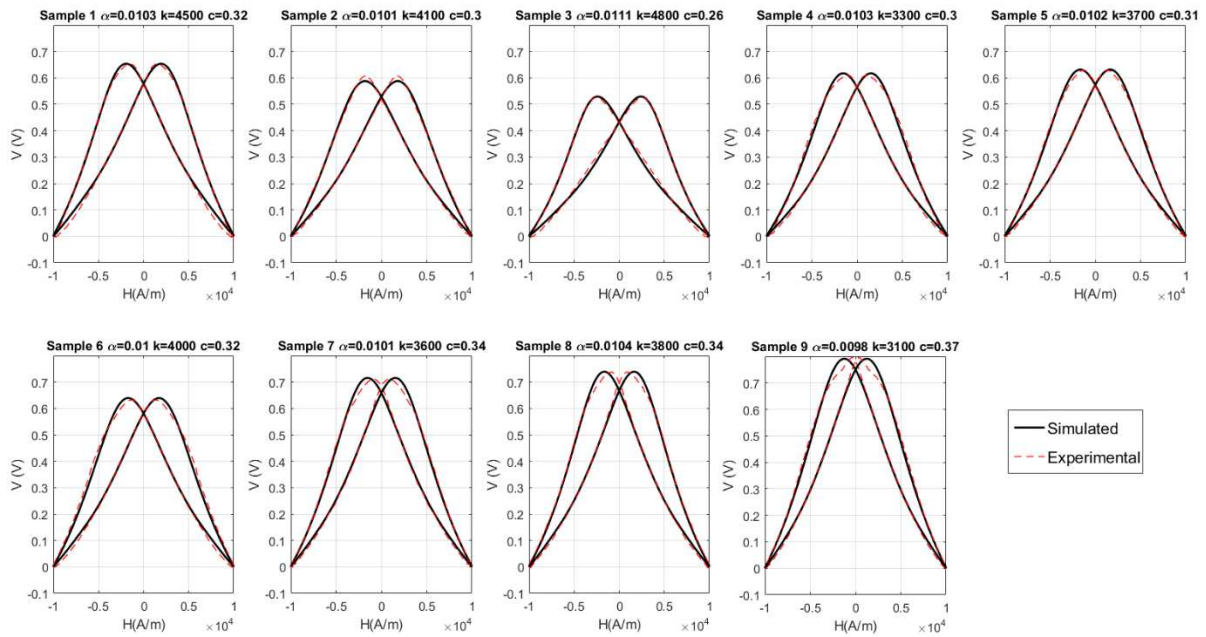
*Corresponding author.

E-mail address: benjamin.ducharne@insa-lyon.fr (Benjamin Ducharne)

406 Here μ^{exp} is the experimental modulus derived from the coil voltage using Eq. (14) and μ^{sim}
 407 the simulated one.

408 Results and discussion

409 Fig. 10 shows below a comparison of the experimental data of the samples with the simulated
 410 ones (V is the modulus of the voltage coil (Eq. 14)). The modeled MIP curves show a
 411 relatively good agreement with the experimental data (small differences can be observed in
 412 the coercivity region). The parameters derived from this process of optimization are then
 413 evaluated against the microstructure of the material, for instance, with number of precipitates
 414 and the average of KAM. Fig. 12 and Fig. 13 show an evaluation of the derived J-A's
 415 parameters against the precipitation number and the average of KAM.



416
 417 *Figure 10: Experimental and simulated MIP curves*

418 4.1. Evolution of the Jiles-Atherton(J-A) parameters versus microstructure

420 4.1.1. J-A parameters vs. Number of Precipitates

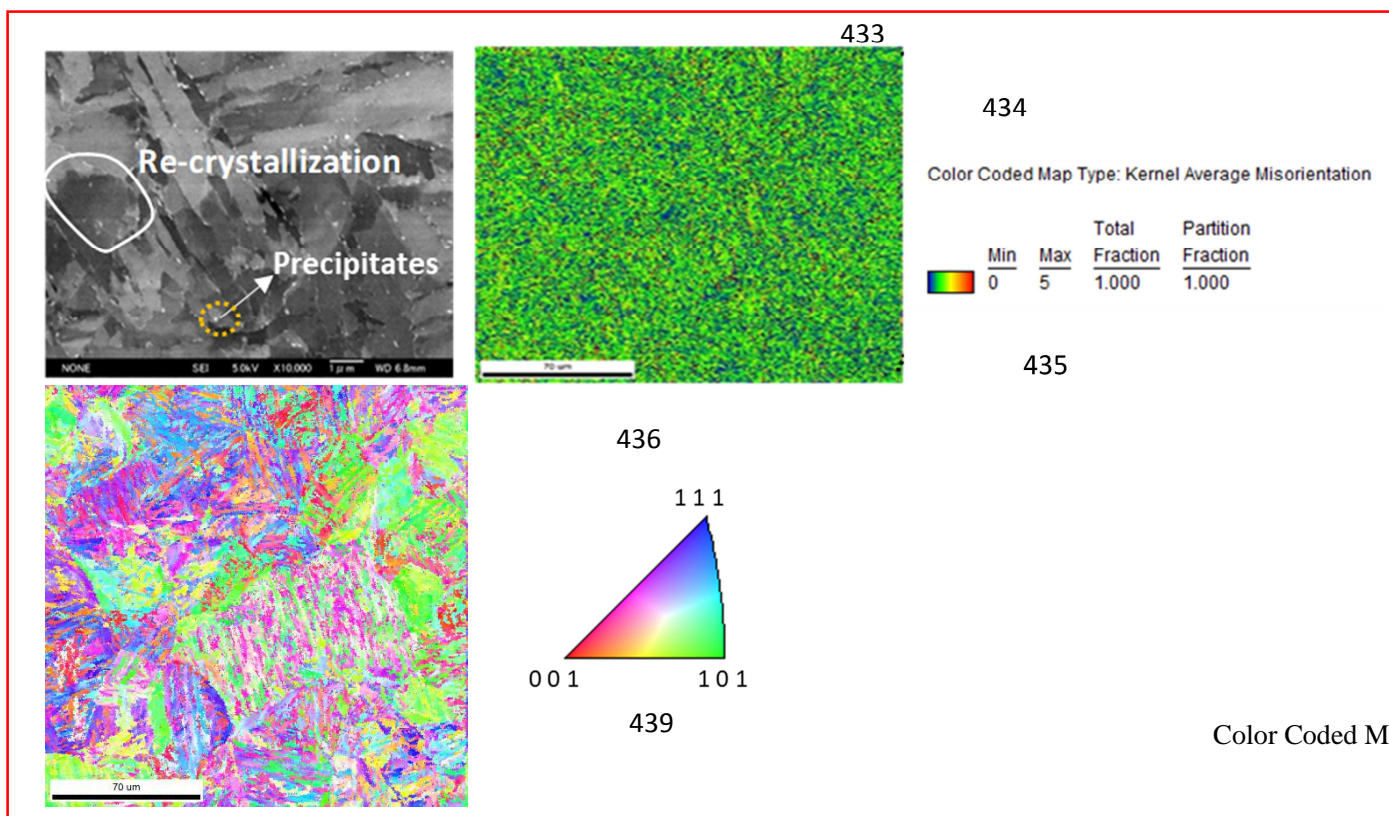
421 Fig.11 show a typical image of microstructural analysis done by Scanning Electron
 422 Microscopy (left) and Kernel Average Misorientation (right) (which can be given by Electron

*Corresponding author.

E-mail address: benjamin.ducharne@insa-lyon.fr (Benjamin Ducharne)

423 Backscattering Diffraction) along with the IPF map that shows the orientation of the crystals.
 424 The regions with bright-contrast in the left image correspond to the precipitates on the sample
 425 surface. The figure shows the number of grains in bright-contrast per unit area ($/\text{mm}^2$). For
 426 the right image in Fig 11, the value of the KAM Average is calculated from the arithmetic
 427 mean associated with the log normal distribution of KAM. **It is estimated that almost all**
 428 **precipitates consist of Cr-Mo carbides. Although the nature of precipitates varies, our**
 429 **procedure (Ar-ion milling / low-acceleration SEM) could detect all precipitates. These data**
 430 **from microstructure are interpreted and also correlated to the mechanical and the magnetic**
 431 **parameters of these samples in the previously published edition of this paper [13].**

432



440

Figure 11: Microstructural Analysis images; SEM(left), KAM(right), IPF orientation map (bottom left) displaying the microstructure of 550 °C ruptured sample

441 Fig.

442 12(a) below shows the evolution of three J-A parameters versus the microstructure of the

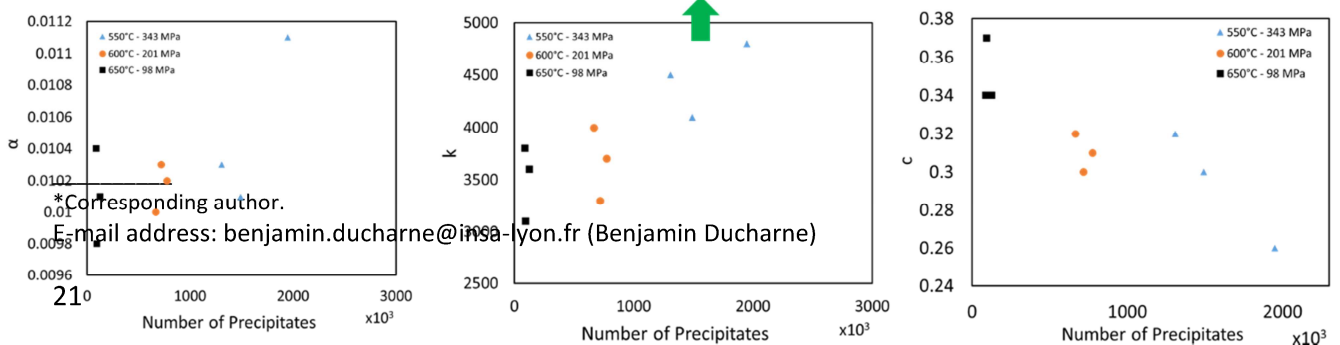
*Corresponding author.

E-mail address: benjamin.ducharne@insa-lyon.fr (Benjamin Ducharne)

443 material. Fig. 12(a) demonstrates the evolution of α which physically represents the inter
 444 domain coupling in the magnetic material. For instance, in the microstructural analysis
 445 (Fig.3), there are a number of precipitates whose size is very small (550°C), which means
 446 that the area of interaction between the domains is **larger** and consequently the inter
 447 domain coupling which is exactly the case in Fig. 12(a). However, on the other hand, the
 448 size of the precipitates for 650°C is very large which decreases the area of interaction
 449 between the domains and hence the inter domain coupling. It has to be noted that when
 450 we discuss about the precipitations per unit area, this effect can be reversed too since, it
 451 depends on the cumulative area of all precipitates and sometimes, total area of the
 452 precipitates combined can be less or more than the total area of the precipitates in 650°C
 453 samples. In that case, the effect can be reversed too in terms of numerical value of alpha.
 454 Similarly, it is the same case in terms of k versus number of precipitates (12(b)). In the
 455 following case, since the number of precipitates and the area combined is much higher in
 456 550°C samples than 650°C samples, the energy required to break the pinning site in the
 457 former category is higher too. This also implies that the percentage of carbide content in
 458 higher temperature treated samples, is much lower than the lower temperature treated
 459 samples cumulatively. When it comes to magnetic reversibility, if the size of the crystals
 460 is higher, and the dislocations are lesser, the original magnetic state of the materials can be
 461 achieved after demagnetization. Alternatively, with bigger size of crystals and lesser
 462 amount of carbide content, it is more difficult to break the pinning site and hence it means
 463 higher magnetic reversibility.

464
 465
 466

Higher the number of precipitates, higher is the energy required to break the pinning site



466
 467
 468
 469

α : inter-domain coupling in the magnetic material
 k: average energy required to break pinning site
 c: magnetization reversibility

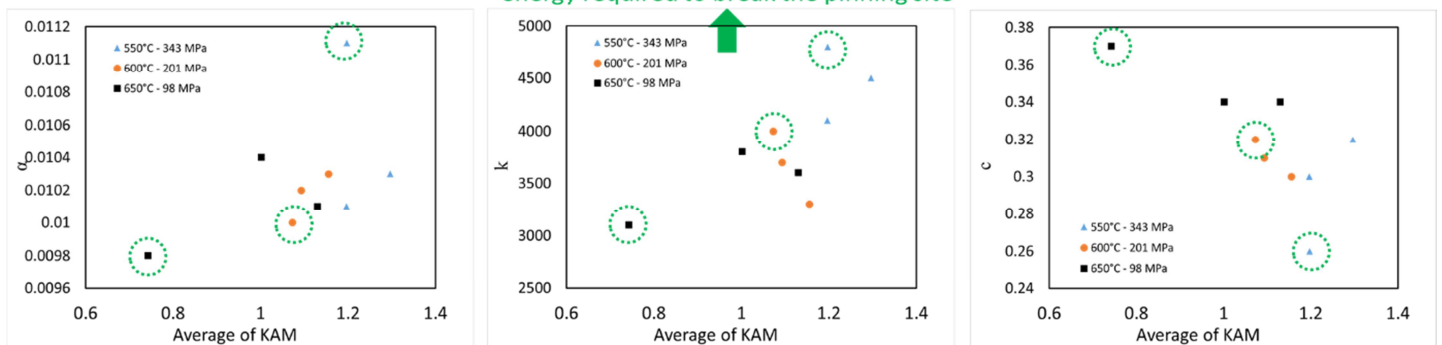
Figure 12: Evolution of J-A parameters vs. Number of Precipitates

471 **Kernel** ⁴⁷⁰_{12(a)} **4.1.2. J-A** ⁴⁷⁰_{12(b)} **parameters vs. Average** ⁴⁷⁰_{12(c)} **of**
 471 **Average** **Misorientation (KAM)**

472 Fig. 13 below shows the evolution of three J-A parameters versus Average of KAM. Fig.
 473 13(a) demonstrates the evolution of alpha which physically represents the inter domain
 474 coupling in the magnetic material. There are a number of dislocations whose size is very
 475 small, which means that the area of interaction between the domains is higher and
 476 consequently the average inter domain coupling. Fig.4 is shown experimentally, that
 477 KAM doesn't show a good co-relation against different magnetic parameters except for
 478 the 650°C samples. As it can be seen in the Fig. below, the J-A parameters also vary more
 479 in case of 650°C samples only. This is probably due to the fact that the crystal size is
 480 bigger and the dislocations are also lesser in comparison to other category of samples.

481

Higher the number of dislocations, higher is the energy required to break the pinning site



482

483 **4.1.3. Pearson Correlation factor**

484 J-A model on fitting with experimental data, gives access to the different parameters. To
 485 understand and validate the parameter, a correlation is checked amongst these parameters

*Corresponding author.

E-mail address: benjamin.ducharne@insa-lyon.fr (Benjamin Ducharne)

Figure 13: Evolution of J-A parameters vs. Average of KAM

486 against various microstructural parameters as shown in Fig. 14. In this study we use Pearson's
487 correlation coefficient which is defined as a measure of the strength of the association
488 between the two variables. Mathematically,

$$489 \quad \rho_{X,Y} = \frac{cov(X,Y)}{\sigma_X \sigma_Y} \quad (17)$$

490 Where, *cov* is the covariance, σ is the standard deviation of the variables (X,Y). In the
491 following figure, different parameters are studied using the data from MIP measurements.
492 Although not detailed in the experimental setup, B(H) curves were determined experimentally
493 on each sample. Based on these measurements J-A parameters were adjusted for each sample
494 as for MIP based experiments. The objective is to be able to assess Pearson correlation
495 coefficient both with MIP and B(H) curves (for B(H) curves, the sample is magnetized at 0.1
496 Hz frequency with a magnitude of 10kA/m and the induced voltage is picked up by a pick-up
497 coil with 50 turns surrounding the sample) and to check the relevance of MIP based
498 determination of J-A parameters. It is worth noticing that the absolute value of correlation
499 factor in case of MIP measurements is close to 1. However, in case of B(H), the correlation is
500 good only in case of α parameter. The possible reason is that the in B(H) measurements, we
501 do not have information about the first magnetization curve which directly relates to magnetic
502 reversibility coefficient, *c*. This also implies that when B(H) measurement is taken, some
503 information about the samples is missing and MIP provides more information about the
504 sample such as reversibility. In other words, variations of *k* and *c* have limited influence of
505 the overall B(H) curve. On the contrary, MIP measurement explores the local permeability
506 with a bias magnetic field, and is therefore much more sensitive to all J-A parameters.

*Corresponding author.

E-mail address: benjamin.ducharne@insa-lyon.fr (Benjamin Ducharne)

507

508

509

510

511

512

513

514

515

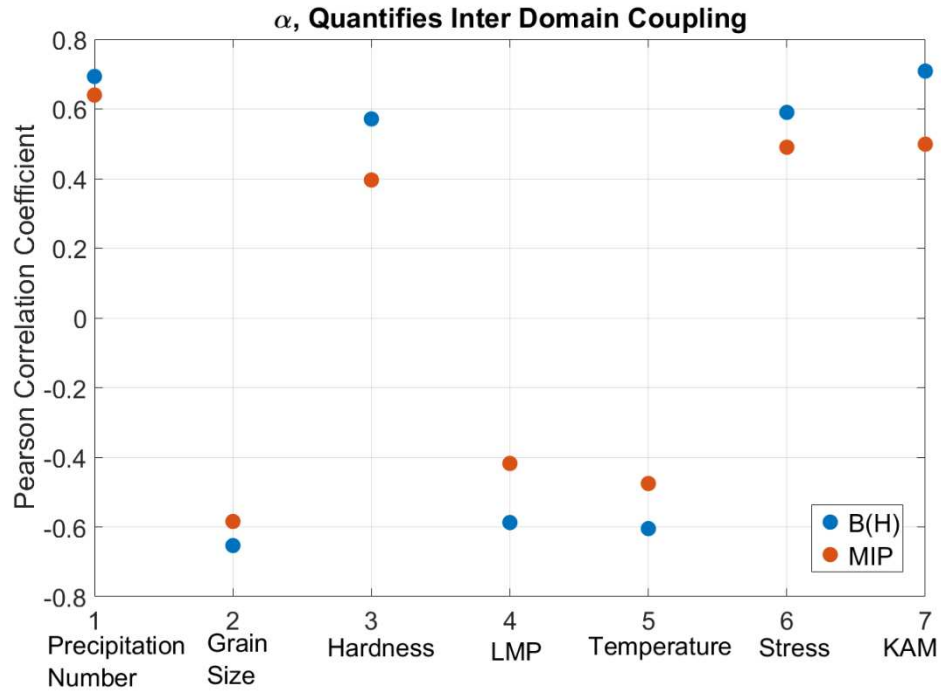


Figure 14(a): Pearson correlation factor for Alpha vs. Microstructural parameters

516

517

518

519

520

521

522

523

524

525

526

527

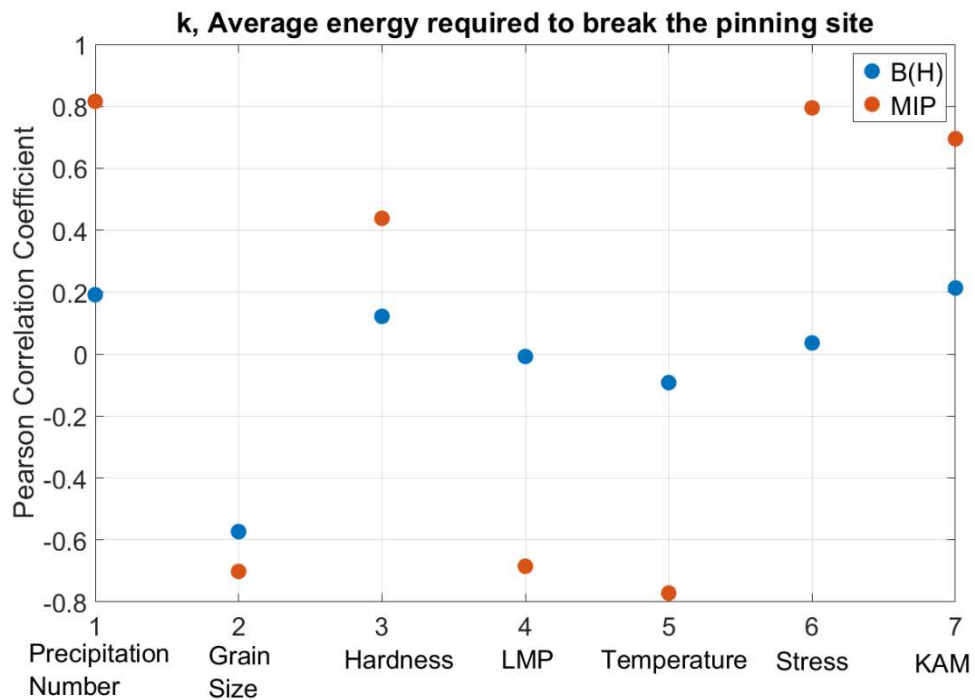


Figure 14(b): Pearson correlation factor for k vs. Microstructural parameters

*Corresponding author.

E-mail address: benjamin.ducharne@insa-lyon.fr (Benjamin Ducharne)

528
529
530
531
532
533
534
535
536
537
538
539
540
541
542
543
544
545
546
547
548
549
550
551

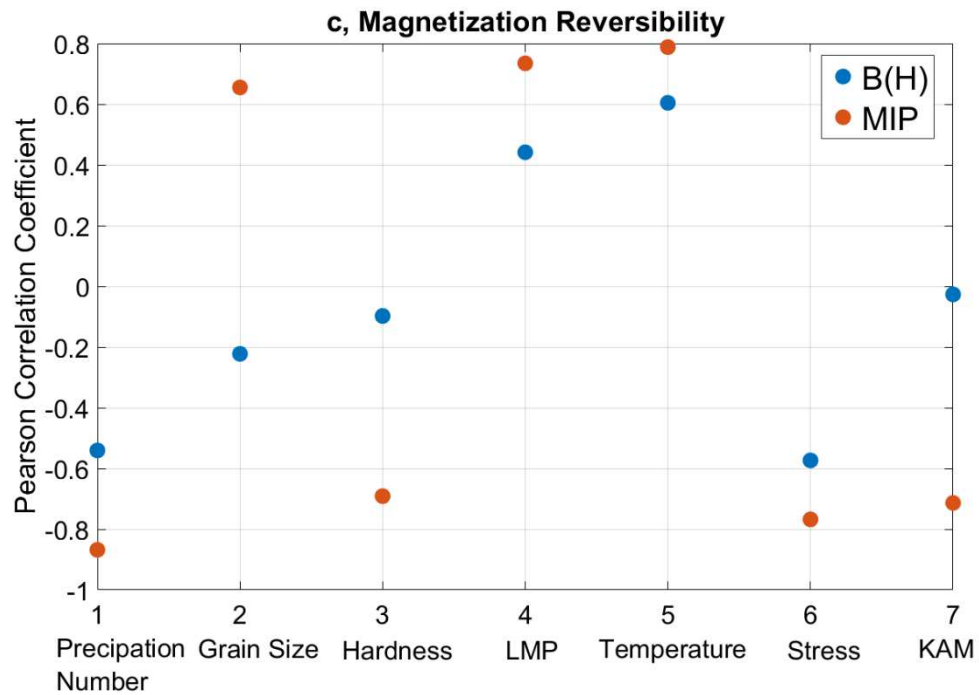


Figure 14(c): Pearson co-relation factor for c vs. Microstructural parameters

4. Conclusion

This work focused on a model based on Jiles-Atherton model to understand more deeply the creep phenomenon on high chromium steel used in thermal power plants. The model derives three parameters which are investigated against the microstructure of the materials. It was observed especially correlations between specific J-A parameters and the number of precipitates (Person correlation coefficient of 0.82), the Kernel Average Misorientation (0.70), the hardness (0.70), and grain size (0.65). Then the physical interpretation of the microstructure is analyzed based on these parameters. The absolute value of these parameters doesn't give information about the microstructure but the tendency and the evolution of these parameters give an idea of creep and degradation of the materials. As a future work, to support this understanding and interpretation, Magnetic Barkhausen Noise tests should be performed and the tendency of these parameters will be studied in relation to MIP measurements and microstructure information.

*Corresponding author.

E-mail address: benjamin.ducharne@insa-lyon.fr (Benjamin Ducharne)

552 **Acknowledgement**

553 The work has been performed in the frame of the Japan - France International Laboratory
554 (LIA) ELYTGlobal. The authors gratefully acknowledge the French Region Auvergne-Rhône-
555 Alpes, the French project IDEXLYON of the Université de Lyon in the frame of the
556 "Investissements d'Avenir" program (ANR-16-IDEX-0005), and the Institute of Fluid
557 Science from Tohoku University through the General Collaborative Program projects #
558 J17I065, and #J18I055.

559

560 **References**

- 561 [1] Sposito,G; A review of non-destructive techniques for the detection of creep
562 damage in power plant steels. NDT&E International. 2010.
- 563 [2] G. Dobmann; Industrial applications of 3MA – Micromagnetic Multiparameter
564 Microstructure and Stress Analysis. Electromagnetic Nondestructive
565 Evaluation (XI). 2008.
- 566 [3] B. Ducharne, B. Gupta, G. Sebald, T. Uchimoto, “Dynamic hysteresis lump
567 model including fractional operators for the incremental permeability
568 nondestructive testing”, Proceeding of the 18th Int. Symp. on Applied
569 Electromag.and Mech. (ISEM), Chamonix, France, 2017.
- 570 [4] P. Meilland, P. Lombard, “Improved Modelling of the 3MA System's
571 Incremental Permeability for on-Line Steel Strip Property Assessment”, in: 19th
572 World Conference on Non-Destructive Testing (WCNDT), Munich, Germany,
573 2016.
- 574 [5] F. Preisach, “Über die magnetische Nachwirkung”. Zeitschrift für Physik, 94:
575 277-302, 1935.

*Corresponding author.

E-mail address: benjamin.ducharne@insa-lyon.fr (Benjamin Ducharne)

- 576 [6] D. C. Jiles and D. L. Atherton, "Theory of ferromagnetic hysteresis", J. Magn.
577 Magn. Mater., vol. 61, no. 1–2, pp. 48–60, Sep. 1986.
- 578 [7] G. Bertotti, "General properties of power losses in soft ferromagnetic
579 materials", IEEE Trans. on Mag., 24, pp. 621-630, 1988.
- 580 [8] Chen H.; Numerical simulation of magnetic incremental permeability for
581 ferromagnetic Material, International Journal of Applied Electromagnetics and
582 Mechanics 45 (2014) 379–386, 2014
- 583 [9] Matsumoto T., Evaluation of chill structure in ductile cast iron by incremental
584 permeability method, International Journal of Applied Electromagnetics and
585 Mechanics 52 (2016) 1599–1605, 2016.
- 586 [10] Mutoh, Y., Improving Fretting Fatigue Strength at Elevated Temperatures by
587 Shot Peening in Steam Turbine Steel, Standardization of Fretting Fatigue Test
588 Methods and Equipment, ASTM STP 1159, M. Helmi Attia and R.B.
589 Waterhouse, Eds., American Society for Testing and Materials, Philadelphia,
590 1992, pp.119-209.
- 591 [11] F. R. Larson & J. Miller, *Transactions ASME*, Vol. 74, p. 765–771, 1952.
- 592 [12] C. Moussa; About quantitative EBSD analysis of deformation and recovery
593 substructures in pure Tantalum bout quantitative EBSD analysis of
594 deformation and recovery substructures in pure Tantalum. 36th Risø
595 International Symposium on Materials Science. 2015.
- 596 [13] B. Gupta, T. Uchimoto, B. Ducharne, G. Sebald, T. Miyazki, T. Takagi, "Magnetic
597 incremental permeability non-destructive evaluation of 12 Cr-Mo-W-V steel

*Corresponding author.

E-mail address: benjamin.ducharne@insa-lyon.fr (Benjamin Ducharne)

- 598 creep samples with varied ageing levels and thermal treatments” NDT & E
599 International, Volume 104, Pages 42-50. 2019.
- 600 [14] Shibli A. Creep and fracture in high temperature components: design and life
601 assessment issues, in: Proceedings of 2nd ECCC creep conference. Lancaster,
602 PA: DEStech Publications; 2009 pp. 402–413.
- 603 [15] Prajapati, S., Potential drop detection of creep damage in the vicinity of
604 welds, NDT & E International, Volume 47, April 2012, Pages 56-65.
- 605 [16] T. Matsumoto, T. Uchimoto, T. Takagi, G. Dobmann, B. Ducharne, S. Oozono, H.
606 Yuya, “Investigation of electromagnetic nondestructive evaluation of residual
607 strain in low carbon steels using the eddy current magnetic signature (EC-MS)
608 metho”, J. of mag. and mag. mat., vol. 479, pp. 212-221, 2019.
- 609 [17] T. Matsumoto, B. Ducharne, T. Uchimoto, “Numerical model of the Eddy
610 Current Magnetic Signature (EC-MS) non-destructive micro-magnetic
611 technique”, AIP Advance, vol. 9, iss. 3, 2019.
- 612 [18] B. Ducharne, G. Sebald, D. Guyomar, G. Litak, “Fractional model of magnetic
613 field penetration into a toroidal soft ferromagnetic sample”, Int. J. of Dyn. And
614 Cont., pp. 1-8, 2017.
- 615 [19] D.C. Jiles, D. L. Atherton, “Theory of ferromagnetic hysteresis”. J. of App.
616 Phys., vol. 55, iss. 6, pp. 2115, 1984.
- 617 [20] D. C. Jiles, “A self consistent generalized model for the calculation of minor
618 loop excursions in the theory of hysteresis,” IEEE Trans. Magn., vol. 28, no. 5,
619 pp. 2602–2604, Sep. 1992.

*Corresponding author.

E-mail address: benjamin.ducharne@insa-lyon.fr (Benjamin Ducharne)

- 620 [21] B. Zhang, B. Gupta, B. Ducharne, G. Sebald, T. Uchimoto, "Dynamic magnetic
621 scalar hysteresis lump model, based on JilesAtherton quasi-static hysteresis
622 model extended with dynamic fractional derivative contribution", IEEE Trans.
623 on. Mag, iss. 99, pp. 1-5, 2018.
- 624 [22] B. Ducharne, D. Guyomar, G. Sebald, "Low frequency modelling of hysteresis
625 behaviour and dielectric permittivity in ferroelectric ceramics under electric
626 field", Journal of Physics D: Applied Physics, vol. 40, iss. 2, pp. 551-555, 2007.
- 627 [23] Langevin P., Comptes Rendues, 1908, vol. 146 pg. 530.
- 628 [24] N. Sadowski, N. J. Batistela, J. P. A. Bastos, M. Lajoie-Mazenc, "An inverse Jiles-
629 Atherton model to take into account hysteresis in time stepping finite element
630 calculations", IEEE Trans. Magn., vol. 38, pp. 797-800, Mar. 2002.
- 631 [25] J. V. Leite, N. Sadowski, P. Kuo-Peng, N. J. Batistela, J. P. A. Bastos, "The inverse
632 Jiles-Atherton hysteresis model parameters identification", IEEE Trans. Magn.,
633 vol. 39, pp. 1397-1400, May 2003.
- 634 [26] Y. Gabi, B. Wolter, A. Gerbershagen, M. Ewen, P. Braun, O. Martins, "FEM
635 simulations of incremental permeability signals of a multi-layer steel with
636 consideration of the hysteretic behavior of each layer", IEEE Trans. On Mag.,
637 vol. 50 n°14, 2014.
- 638 [27] Y. Gabi, A. Kedous-Lebouc, G. Meunier, B. Wolter, O. Geoffroy, P. Meilland, P.
639 Labie, C. Guérin, O. Martins, "Assessment of 3MA technique potentiality for
640 nondestructive evaluation of dual-phase steels using 2-D nonlinear FEM and
641 taking hysteretic behavior into account", *Proc. 19th Conf. Comput.*
642 *Electromagn. Fields*, pp. 48-48, Jul. 2013.

*Corresponding author.

E-mail address: benjamin.ducharne@insa-lyon.fr (Benjamin Ducharne)